Supporting Information

Highly selective one-step CO_2 conversion to liquid alcohols through plasma synergistic MOFs catalysis

Chong Qi[a,b†], Pengchen He[a†], Yuan Gao[a], Dengke Xi[a], Yuxuan Xu[a,b], Liguang Dou[a], Li Lv[a,c], Cheng Zhang[a,b], Tao Shao*[a,b]

[a] Beijing International S&T Cooperation Base for Plasma Science and Energy Conversion, Institute of Electrical Engineering, Chinese Academy of Sciences, Beijing 100190, China

[b] University of Chinese Academy of Sciences, Beijing 100049, China

[c] Hefei University of Technology, Anhui 230009, China

*Corresponding authors

Email: st@mail.iee.ac.cn

[†]Chong Qi and Pengchen He contributed equally to this work.

Contents

1. Characterization of fresh X% Co/Cu-BDC-NH_2

2. Electrical characterization

3. ^{1}HNMR spectra of major liquid products

4. Catalyst stability results

5. Characterization of spent catalysts

6. CO_2-TPD results

7. CO-DRIFTS characterization results

8. Plasma-coupled in-situ infrared spectroscopy results

9. Supplementary tables

1. Characterization of fresh X% Co/Cu-BDC-NH_2

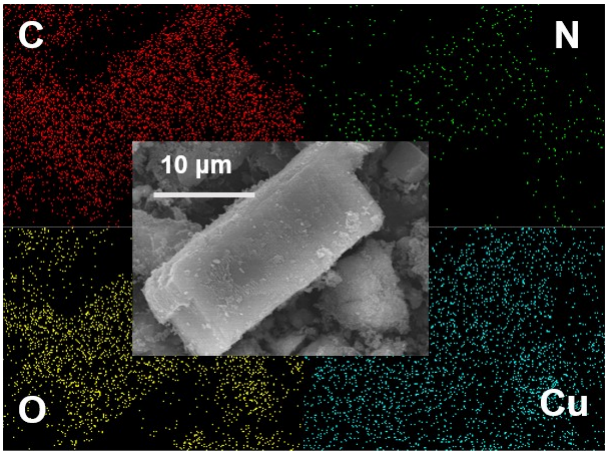

Figure S1. Scanning electron microscope (SEM) images of Cu-BDC-NH_2 and SEM mapping of Cu-BDC-NH_2.

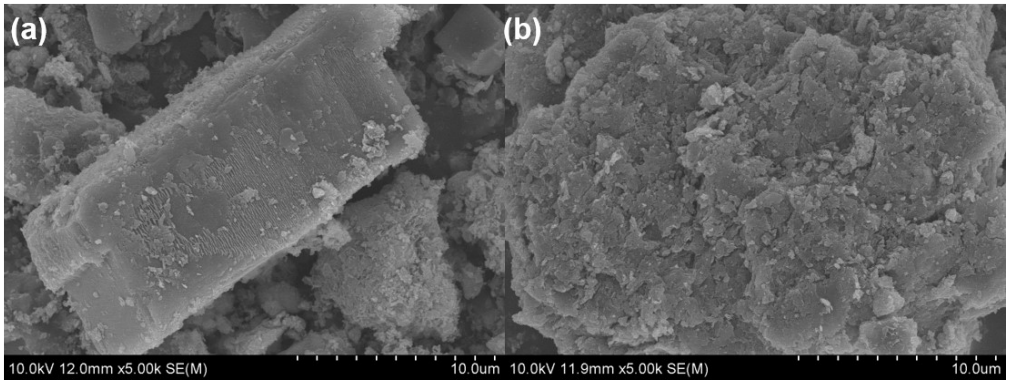

Figure S2. SEM images of (a) Cu-BDC-NH_2 and (b) 10% Co/Cu-BDC-NH_2.

Table S1. Inductively coupled plasma optical emission spectrometry (ICP-OES) analysis of 5% Co/Cu-BDC-NH_2, 10% Co/Cu-BDC-NH_2 and 15% Co/Cu-BDC-NH_2.

Catalyst	Co content (wt%)
5% Co/Cu-BDC-NH_2	4.4
10% Co/Cu-BDC-NH_2	8.5
15% Co/Cu-BDC-NH_2	14.2

Table S2. S_{BET}, pore volume and pore diameter of fresh catalysts.

Samples	S_{BET}[a] (m^2/g)	Pore volume[b] (cm^3/g)	Pore diameter[c] (nm)
Cu-BDC-NH_2	24.5	0.06	10.5
10% Co/Cu-BDC-NH_2	10.4	0.06	21.6

[a]The Brunauer-Emmett-Teller (BET) method was used to determine the specific surface area of samples.

[b]The single point method (at $p/p^0 = 0.99$) was used to determine the total pore volume.

[c]The BJH method was used to determine the average pore diameter.

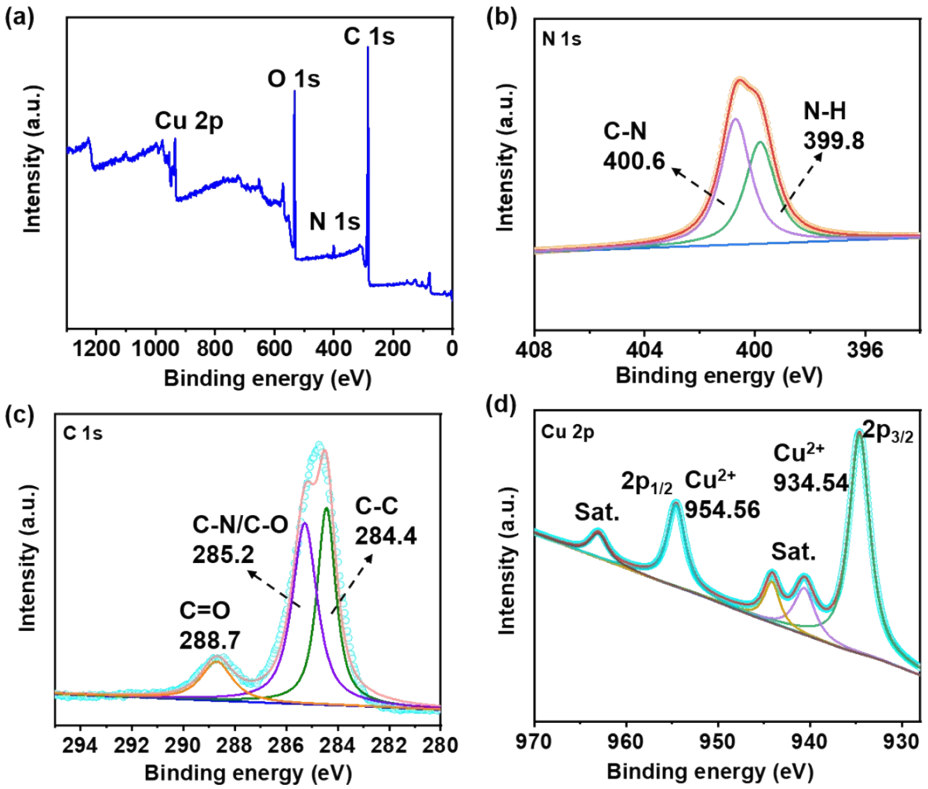

Figure S3. (a) Survey XPS spectra, (b) N1s XPS profiles, (c) C1s XPS profiles and (d) Cu 2p XPS profiles of Cu-BDC-NH_2.

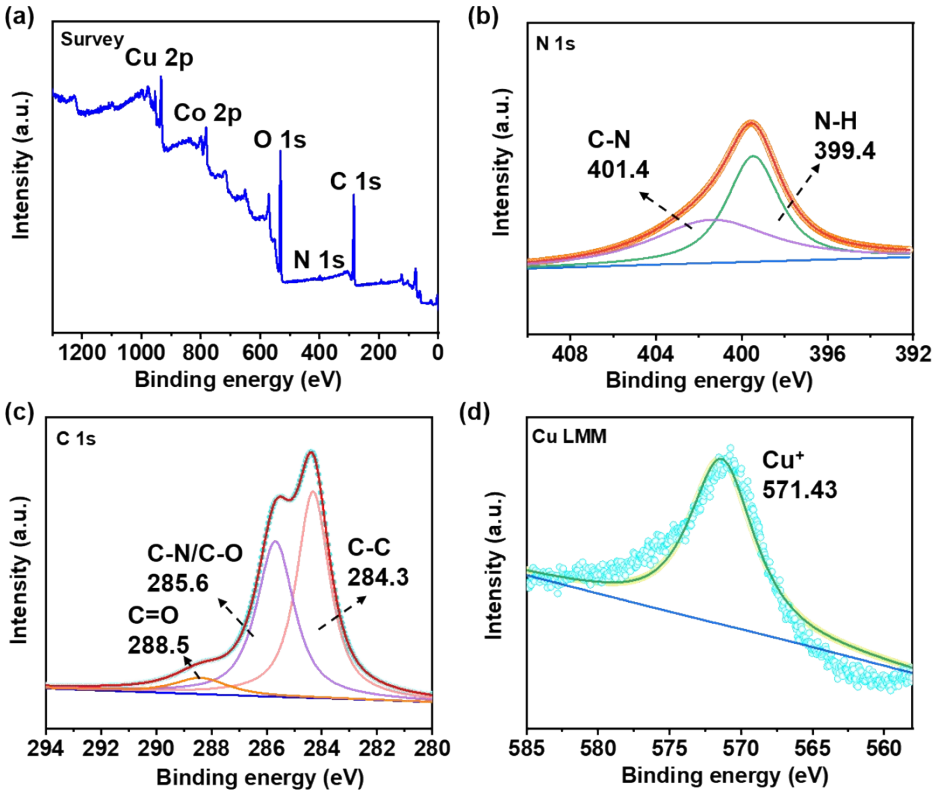

1

2 **Figure S4**. (a) Survey XPS spectra, (b) N1s XPS profiles, (c) C1s XPS profiles and (d)

3 Auger Cu LMM spectrum of 10% Co/Cu-BDC-NH_2.

4

2. Electrical characterization

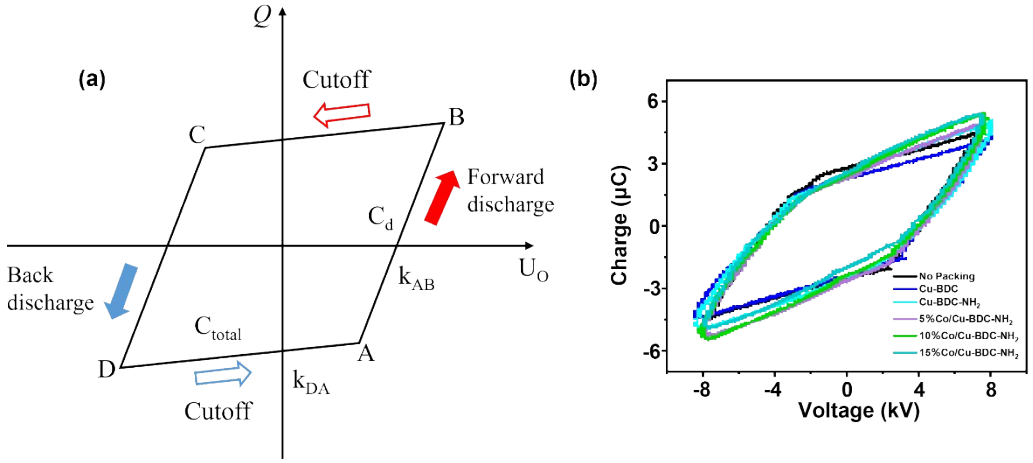

Figure S5. (a) The standard Lissajous figures and (b) the actual measured Lissajous figure.

Within each cycle of the sinusoidal voltage excitation, the gas gap in the dielectric barrier discharge (DBD) reactor underdoes two breakdown and two quenching events. When the applied voltage rises positively to the breakdown threshold, the gap breaks down and discharges, entering a conducting state, during which the voltage amplitude decreases. After the discharge quenches, the voltage continues to follow the sinusoidal waveform. An identical process occurs during the negative half-cycle. According to its equivalent circuit model (**Figure S5a**), the entire system can be represented by the series combination of the dielectric capacitor (C_d) and the gap capacitor (C_g) when the gas gap is not broken. Upon breakdown, the gap behaves as a short circuit, leaving only the dielectric capacitor in the circuit. This physical process manifests as linear segments with different slopes in the Lissajous figure. The slope of each linear segment in the figure has a clear physical meaning: it directly corresponds to the instantaneous equivalent capacitance of the system in that specific state. Specifically, the discharge stage (AB and CD section), and its slope corresponds to the dielectric capacitance C_d. The cut-off stage (DA and BC segments), and its slope corresponds to the total capacitance C_{total} of the system.

$$C_d = k_{AB} \quad \text{(S1)}$$

$$C_{total} = k_{DA} \quad \text{(S2)}$$

Based on the series relationship of capacitors, the gap capacitance C_g can be calculated:

$$C_g = \frac{C_d \times C_{total}}{C_d - C_{total}} \quad \text{(S3)}$$

According to **Table S3**, the system capacitance increased progressively from 28.5 pF (no catalyst) to 62.6 pF (15% Co/Cu-BDC-NH_2) with catalyst filling, while the discharge power varied between 22.4 W and 26.7 W.

Table S3. Capacitances properties

Sample	C_d (pF)	C_{total} (pF)	C_g (pF)	P (W)
Plasma	132.2±1.0	23.5±1.0	28.5±1.0	23.4
Cu-BDC	114.4±2.0	24.1±1.0	30.5±1.0	25.8
Cu-BDC-NH_2	111.1±1.0	31.4±2.0	43.7±1.0	22.4
5%Co/ Cu-BDC-NH_2	110.5±1.0	34.8±1.0	50.8±1.0	25.6
10%Co/ Cu-BDC-NH_2	117.3±1.0	38.8±2.0	57.9±1.0	25.1
15%Co/ Cu-BDC-NH_2	120.2±1.0	41.2±1.0	62.6±1.0	26.7

3. ^{1}HNMR spectra of major liquid products

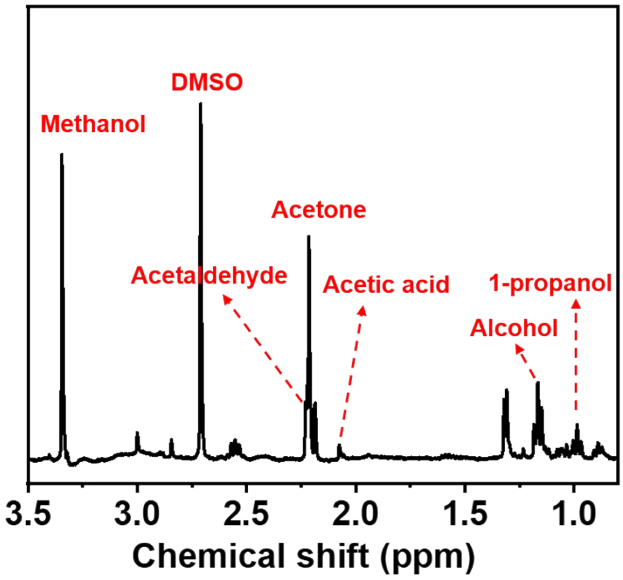

Figure S6. ^{1}HNMR spectra of major liquid products.

4. Catalyst stability results

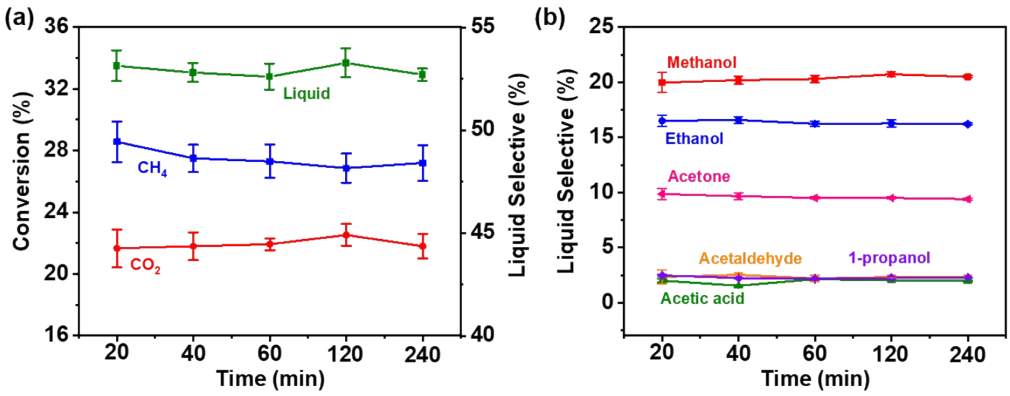

Figure S7. Catalyst stability using 10% Co/Cu-BDC-NH_2 (a) gas conversion and total liquid selectivity and (b) selectivity of main liquid products over time on stream.

5. Characterization of spent catalysts

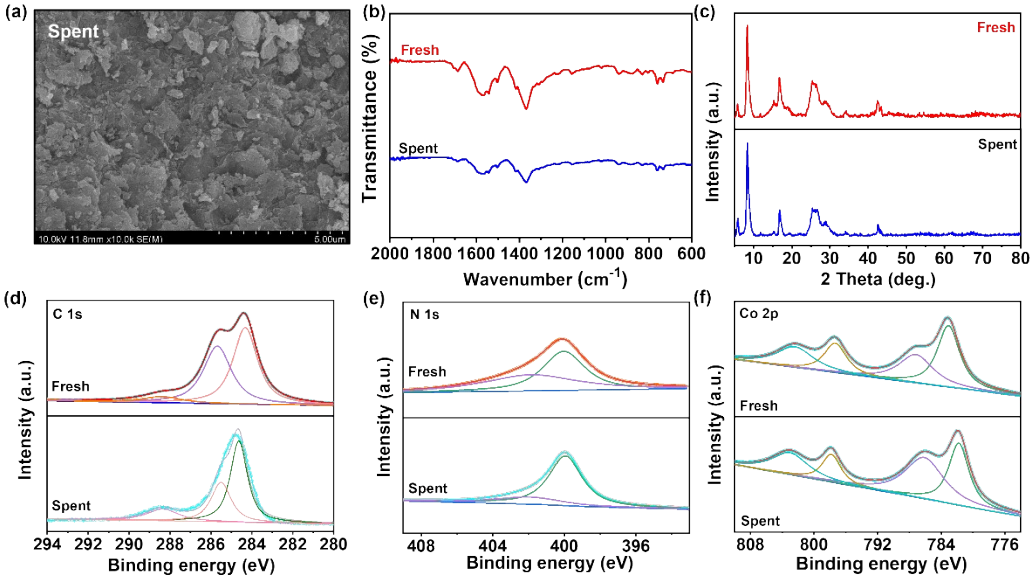

Figure S8. Characterization of fresh and spent 10% Co/Cu-BDC-NH_2 (a) SEM images (b) FTIR spectra and (c) XRD patterns. XPS spectra of (d) C 1s (e) N 1s and (f) Co 2p.

A comparison of the FTIR spectra before and after the reaction revealed the peak positions and shapes remained largely identical, while the intensities changed significantly. The high consistency in peak position and shape indicated that the main framework, core functional groups, and local chemical environment of the catalyst were not irreversibly altered or substantially degraded, preliminarily confirming its good chemical and structure stability. In contrast, the significant changes in absorption intensity suggested an evolution in the catalyst's physical state. This was supported by XRD analysis, which showed a slight decrease in the crystallinity of the catalyst after reaction. The reduction in long-range order directly affected the infrared absorption efficiency of lattice vibrations, leading to an overall weakening of the characteristic peak intensity. Therefore, the observed spectral intensity changes were attributed primarily to the evolution of the catalyst's physical structure — such as its crystallinity and micro-ordering — rather than to any fundamental change in its chemical composition.

Analysis of the C1s XPS spectra before and after reaction showed that the intensity of C-C/C-H peak at 284.3 eV remained unchanged. This indicated that the basic carbon skeleton of the catalyst remained stable during the reforming reaction, without significant consumption or coverage. Concurrently, a decrease in the intensity of the C-N/C-O peak at 285.6 eV was observed, while that of the C=O peak at 288.5 eV increased. This change was likely due to the formation of carbonyl-rich (C=O) intermediate or oxygen-containing species during the reaction, which became strongly adsorbed or chemically bonded to the catalyst surface, thereby directly enhancing the C=O signal. This inference was further corroborated by the corresponding C=O signatures observed via plasma-coupled in-suit infrared spectroscopy. Moreover, analysis of the post-reaction N 1s spectrum revealed a reduction in the C-N peak at 401.4 eV, consistent with the decrease noted in the C 1s spectrum.

6. CO_2-TPD results

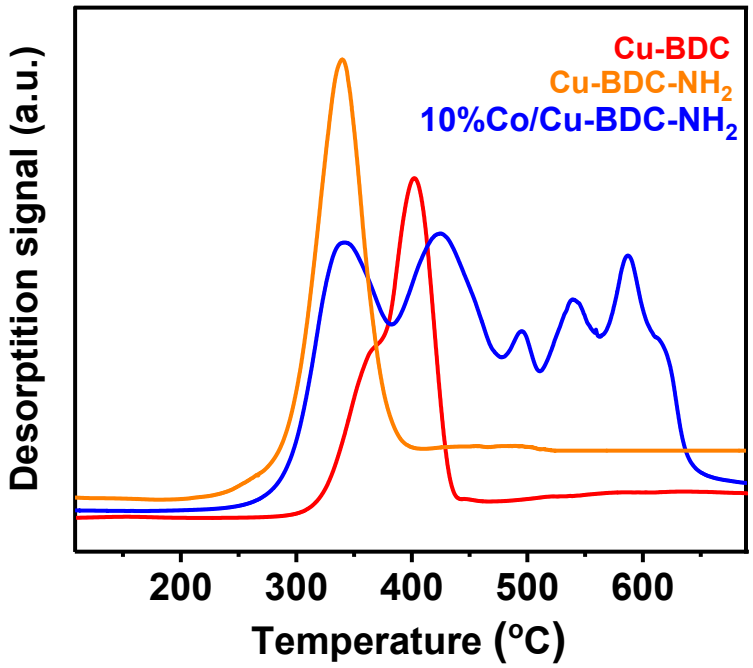

Figure S9. CO_2-TPD of Cu-BDC, Cu-BDC-NH_2 and 10% Co/Cu-BDC-NH_2.

As shown, Cu-BDC-NH_2 exhibited higher CO_2 adsorption capacity than pristine Cu-BDC, confirming that -NH_2 functionalization enhanced CO_2 capture and promoted its conversion. SEM and TEM analysis indicated that Co exists in the form of nanoparticles. These nanoparticles not only exposed abundant strong Lewis basic sites but also directly interacted with CO_2 to form stable carbonate species that require higher temperature for desorption. Furthermore, the introduction of Co may induce local structural reconstruction of the support, generating defects such as coordination unsaturated metal sites or oxygen vacancies. These defect sites typically exhibited a strong affinity for CO_2 adsorption. Consequently, Co loading directly introduced a new strongly basic active phase and indirectly created highly active defect sites. This dual effect resulted in the appearance of a significant additional adsorption peak in the high temperature region of the CO_2-TPD profile.

7. CO-DRIFTS characterization results

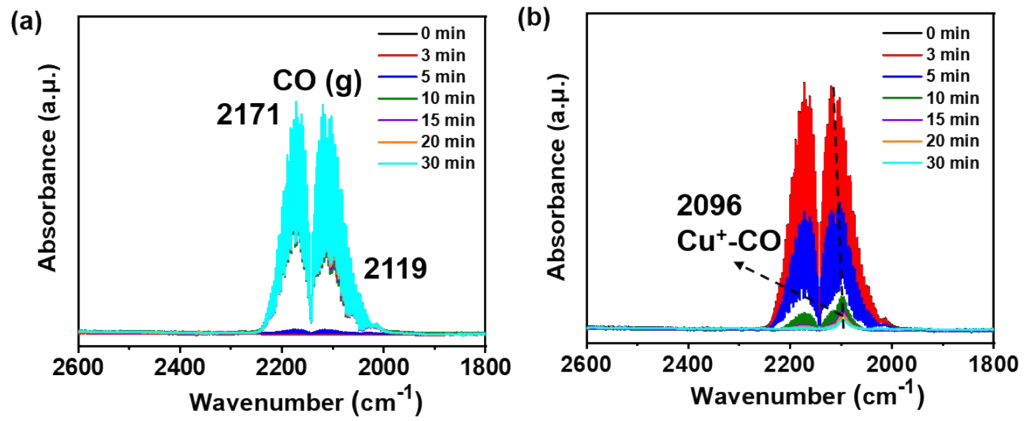

Figure S10. (a) DRIFT spectra of Cu-BDC-NH_2 during CO adsorption. (b) DRIFT spectra of Cu-BDC-NH_2 after CO adsorption with subsequent Ar flush.

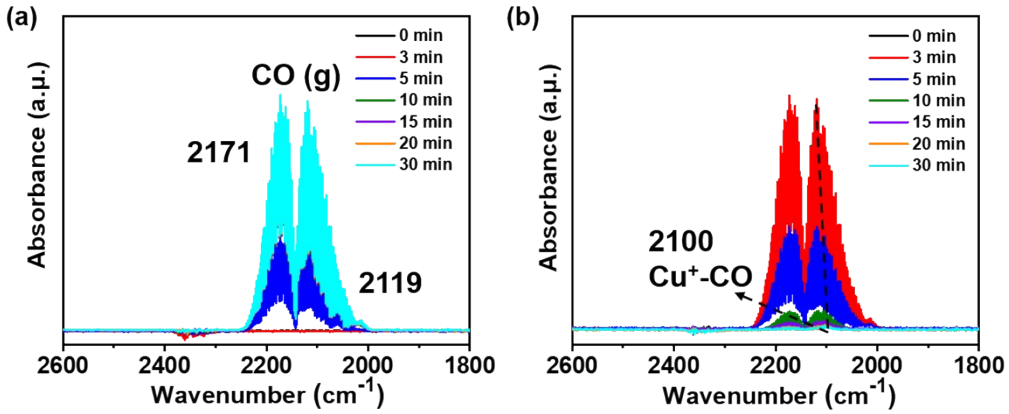

Figure S11. (a) DRIFT spectra of 10% Co/Cu-BDC-NH_2 during CO adsorption. (b) DRIFT spectra of 10% Co/Cu-BDC-NH_2 after CO adsorption with subsequent Ar flush.

8. Plasma-coupled in-situ infrared spectroscopy results

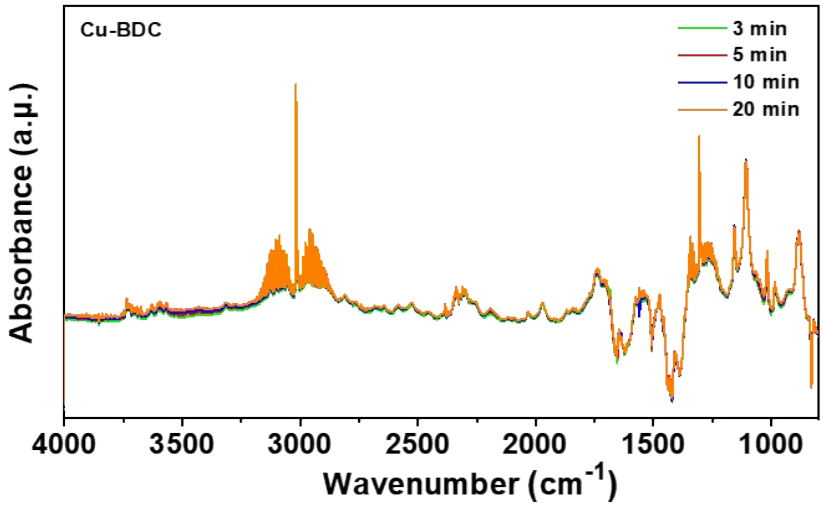

Figure S12. Plasma-coupled in-situ infrared spectroscopy of Cu-BDC during plasma-catalytic DRM reaction (CO_2/CH_4 = 1:1, total gas flow rate = 30 mL/min, discharge power = 20 W)

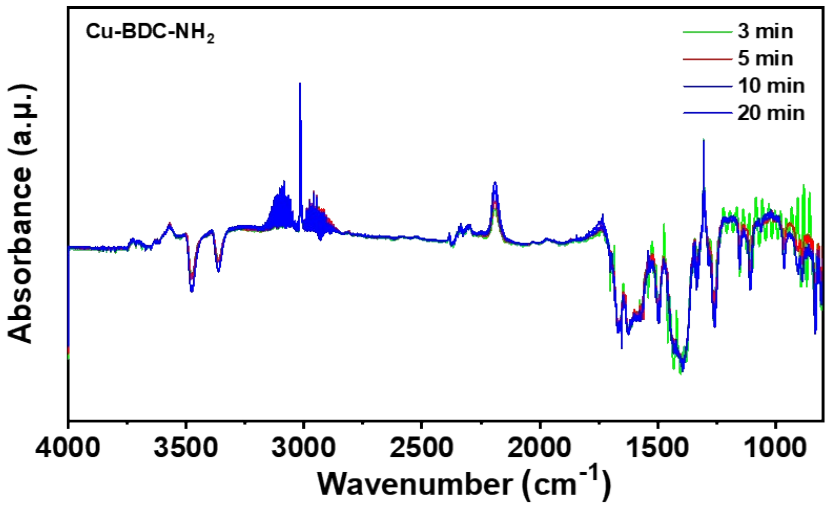

Figure S13. Plasma-coupled in-situ infrared spectroscopy of Cu-BDC-NH_2 during plasma-catalytic DRM reaction (CO_2/CH_4 = 1:1, total gas flow rate = 30 mL/min, discharge power = 20 W)

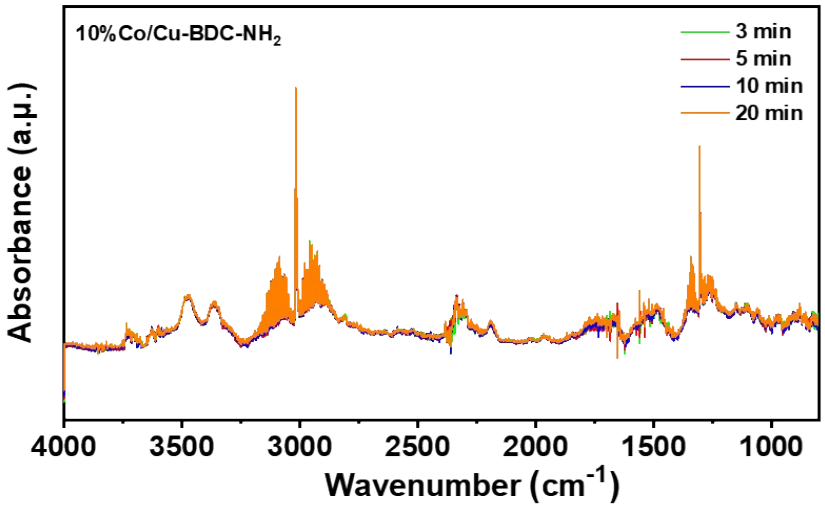

Figure S14. Plasma-coupled in-situ infrared spectroscopy of 10% Co/Cu-BDC-NH_2 during plasma-catalytic DRM reaction (CO_2/CH_4 = 1:1, total gas flow rate = 30 mL/min, discharge power = 20 W)

9. Supplementary tables

Table S4. Effect of catalysts on the conversion and total liquid selectivity (total flow rate = 40 mL/min, discharge power = 25 W).

Sample	CO_2 (%)	CH_4 (%)	Total liquid selectivity (%)	C balance (%)
No packing	15.7	20.6	21.3	96
Cu-BDC	18.3	23.7	43.1	97
Cu-BDC-NH_2	19.6	24.9	45.4	98
5% Co/Cu-BDC-NH_2	19.1	24.4	48.3	97
10% Co/Cu-BDC-NH_2	22.7	27.1	53.9	98
15% Co/Cu-BDC-NH_2	18.6	24.5	40.1	96

Table S5. Effect of catalysts on the selectivity of gas products (total flow rate = 40 mL/min, discharge power = 25 W).

Sample	H_2 (%)	CO (%)	C_2H_6 (%)	C_2H_4 (%)	C_3H_8 (%)	C_3H_6 (%)	C_4H_{10} (%)
No packing	29.3	36.1	26.6	8.4	5	0.08	2.7
Cu-BDC	23.1	28.3	21.1	1	4.3	0.07	2.2
Cu-BDC-NH_2	23.4	26.8	20.1	0.9	4.5	0.07	2.3
5% Co/Cu-BDC-NH_2	23.2	25.5	19.2	0.9	3.9	0.06	1.8
10% Co/Cu-BDC-NH_2	20.2	22.3	17.5	0.6	3.9	0.08	1.8
15% Co/Cu-BDC-NH_2	25.8	29.9	21.3	1.2	4.6	0.1	2.3

Table S6. Effect of catalysts on the selectivity of liquid products (total flow rate = 40 mL/min, discharge power = 25 W).

Samples	CH_3OH (%)	C_2H_5O (%)	CH_3COOH (%)	CH_3CHO (%)	C_3H_7OH (%)	C_3H_6O (%)
No packing	8.6	4.6	0.7	0.9	1.6	4.5
Cu-BDC	13.4	10.6	0.5	2.2	4.8	11.6
Cu-BDC-NH_2	18.7	8.6	0.9	2.1	3.6	11.7
5% Co/Cu-BDC-NH_2	16.1	10.7	1.2	2.5	4.4	13.4
10% Co/Cu-BDC-NH_2	20	16.5	2.3	2.3	2.5	9.9
15% Co/Cu-BDC-NH_2	16.3	11.2	0.9	1.9	2.2	7.2

Table S7. Time-on-stream stability of 10% Co/Cu-BDC-NH_2 about conversion and total liquid selectivity.

Time (min)	CO_2 (%)	CH_4 (%)	Total liquid selectivity (%)
20	21.7	28.6	53.1
40	21.8	27.5	52.8
60	21.9	27.3	52.6
120	22.5	26.9	53.2
240	21.8	27.2	52.8

Table S8. Time-on-stream stability of 10% Co/Cu-BDC-NH_2 about selectivity of liquid products (Total flow: 40 mL min^{-1}, Discharge power: 25 W) (average value).

Time (min)	CH_3OH (%)	C_2H_5OH (%)	CH_3COOH (%)	CH_3CHO (%)	C_3H_7OH (%)	C_3H_6O (%)
20	20.0	16.5	2	2.3	2.5	9.9
40	20.2	16.6	1.5	2.5	2.2	9.7
60	20.3	16.2	2.1	2.2	2.2	9.8
120	20.7	16.3	2.0	2.3	2.2	9.5
240	20.5	16.2	2.0	2.3	2.3	9.4

Table S9. Spectroscopic characteristics of the main species detected in the CO_2-CH_4 plasma.

Species	Electron transition	Wavelength (nm)	Reference
CO	$b^3\Sigma_{2u}$-$a^3\Pi_{1g}$	283.4	[1], [2]
		296.6	[1], [2]
CO^+	$B^2\Sigma$-$X^2\Sigma$	288.8	[1]
CO_2^+	$A^2\Pi_u$-$X^2\Pi_g$	305.8	[1], [7]
		327	[1], [7]
		351.8	[6], [7]
		368.3	[6], [7]
CH	$A^2\Delta$-$X^2\Pi$	431.4	[6], [2], [3], [4]
	$B^2\Sigma$-$X^2\Pi$	388.2	[6], [2], [4]
	$C^2\Sigma^+$-$X^2\Pi$	314.6	[6], [7], [4]
CO	$B^1\Sigma$-$A^1\Pi$ (Angstrom system)	450.7	[6], [8]
		483	[6], [8]
		520	[6], [8]
		559.3	[6], [8]
		608.1	[6], [8]
C_2	$d^2\Pi$-$a^3\Pi$ (Swan)	469.4	[6], [7]
		471.5	[6], [7]
		516.8	[6], [7], [3]
H_α	3d-2p	656.3	[6], [7]

Table S10. Species identified in the plasma-catalytic DRM reaction over 10% Co/Cu-BDC-NH_2 by plasma-coupled in-situ infrared spectroscopy.

Species	Assignment	Wavenumber (cm^{-1})	Reference
Alcohols	C-O stretching vibration	1016	5
*CH_3O	H-C=O bending vibration	1106	6, 7
*CH_3O	C-O stretching vibration	1157	8, 9
Bidentate carbonates		1306	10, 11
Monodentate carbonates		1480	10, 12
-NH_2COOH	C=O stretching vibration	1730	13,14
*CO	Bridging CO adsorbed	1970	15, 16
*CO	Linear CO adsorbed	2032	15, 17, 18
CO (g)		2190	19, 20
CO_2 (g)		2362	21, 22
*HCOO		2642	23
*CH_3	C-H stretching vibration	2810	24,25
CH_4 (g)		3016	26
Surface OH	O-H stretching vibration	3364	27
Isolated OH	O-H stretching vibration	3566, 3600, 3625	28,29
CO_2 (g)	Overtone of CO_2	3725	21

Table S11. Summary of conversions and liquid selectivity reported in the literature.

Reference	CO_2 (%)	CH_4 (%)	Total liquid selectivity (%)	Alcohols selectivity (%)
[30]	18	22	40.1	35
[31]	30.2	34.7	55	38.3
[32]	~12.2	~22	~25	~10
[33]	~7.3	~11.6	~25	~19
[34]	~7	~17	~45	~38
This work	22.7	27.1	53.9	38.9

Table S12. Summary of mechanisms and strategies reported in the literature.

Reference	Strategy	Mechanism
[30]	DBD reactor AC power	1. Methanol is formed mainly via CH_3 coupling with OH radicals. 2. The pathway is enabled by efficient CO_2 activation and OH radical enrichment, both driven by the iron active species.
[31]	DBD reactor AC power	1. Liquid product formation proceeds via stepwise CO hydrogenation coupled with CH_x and OH radical coupling. 2. This mechanism is facilitated by the high-performance catalyst prepared through the grinding method.
[32]	DBD reactor AC power	1. The prepared CuSA-CN catalyst's well-defined Cu–N_4 single-atom sites enable acetic acid synthesis via a bidirectional mechanism. 2. The charge transfer between metal and support facilitates reactant activation, while the sites also

		lower the energy barriers for key steps like CH_4 dissociation and C–C coupling.
[33]	DBD reactor AC power	1. Water participates as a reactant, cooperating with the copper catalyst to promote CH_3 and OH coupling into methanol 2. Water facilitates methanol desorption from the catalyst surface, enhancing efficiency and preventing over-conversion.
[34]	DBD reactor AC power	1. In plasma-catalyzed DRM, copper valence state and loading jointly determine alcohol product distribution. 2. Cu^{2+} species enhance alcohol selectivity, while increased copper loading shifts the major product from methanol to ethanol.
This work	DBD reactor AC power	1. The Co/Cu-BDC-NH_2 catalyst enhances CO_2 adsorption via basic -NH_2 groups and improves CO utilization with loaded Co. 2. Its mechanism acts as a "molecular shunt switch" to dynamically regulate the reaction pathway. 3. -NH_2 functionalization shifts the route from stepwise CO hydrogenation toward OH/CHx coupling. Co addition then reverses this shift, restoring CO hydrogenation as the main pathway. Co and -NH_2 also work together to regulate CH_3O intermediate formation and consumption.

Building upon the established mechanism by which metal active sites or metallic oxide active sites mediate the coupling of CH_x and OH radicals to form oxygenated products, this study proposed a novel catalyst design strategy. The synthesized Co/Cu-

BDC-NH_2 material enabled dynamic modulation of the reaction pathway through the introduction of $–NH_2$ groups and Co species. Their synergistic interaction likely allowed more flexible regulation of key intermediates, thereby endowing the catalyst with enhanced CO_2 conversion efficiency and improved product selectivity.

References

1. Y. Wang, Y. Chen, J. Harding, H. He, A. Bogaerts and X. Tu, *Chem. Eng. J.*, 2022, **450**, 137860.
2. X. Wang, Y. Gao, S. Zhang, H. Sun, J. Li and T. Shao, *Appl. Energ.*, 2019, **243**, 132-144.
3. X. Zhang, Y. Wenren, W. Zhou, J. Han, H. Lu, Z. Zhu, Z. Wu and M. S. Cha, *J. Phys. D Appl. Phys.*, 2020, **53**, 194002.
4. Y. Gao, L. Dou, B. Feng, C. Zhang and T. Shao, *Energ. Convers. Manage.*, 2023, **276**, 116570.
5. J. Shi, C. Mahr, M. M. Murshed, T. M. Gesing, A. Rosenauer, M. Bäumer and A. Wittstock, *Phys. Chem. Chem. Phys.*, 2017, **19**, 8880-8888.
6. Q. Zhang, S. Wang, X. Shi, M. Dong, J. Chen, J. Zhang, J. Wang and W. Fan, *Appl. Catal. B Environ.*, 2024, **346**, 123748.
7. J. Li, W. Pan, Q. Liu, Z. Chen, Z. Chen, X. Feng and H. Chen, *J. Am. Chem. Soc.*, 2021, **143**, 6551-6559.
8. S. Deng, N. Wang, Y. Zhu and K. Thummavichai, *Catal. Sci. Technol.*, 2024, **14**, 6443-6465.
9. P. Liu, Z. Huang, X. Gao, X. Hong, J. Zhu, G. Wang, Y. Wu, J. Zeng and X. Zheng, *Adv Mater.*, 2022, **34**, e2200057.
10. H. Ren, H. Yang, J. Xin, C. Wu, H. Wang, J. Zhang, X. Bu, G. Yang, J. Li, Y. Sun and P. Gao, *Appl. Catal. B Environ.*, 2024, **358**, 124440.
11. M. Zhao, J. Deng, J. Liu, Y. Li, J. Liu, Z. Duan, J. Xiong, Z. Zhao, Y. Wei, W. Song and Y. Sun, *ACS Catal.*, 2019, **9**, 7548-7567.
12. J. Hu, Y. Li, Y. Zhen, M. Chen and H. Wan, *Chin. J. Catal.*, 2021, **42**, 367-375.
13. S.-C. Yang, S. H. Pang, T. P. Sulmonetti, W.-N. Su, J.-F. Lee, B.-J. Hwang and C. W. Jones, *ACS Catal.*, 2018, **8**, 12056-12066.
14. Z. Bacsik, N. Ahlsten, A. Ziadi, G. Zhao, A. E. Garcia-Bennett, B. Martín-Matute and N. Hedin, *Langmuir*, 2011, **27**, 11118-11128.

15. H. Sun, J. Lv, C. Wang, Y. Zhang, S. Sun, P. Zhang, G. Cheng, D. Mei, Y. Wang and Z. Yan, *Fuel*, 2025, **381**, 133413.
16. X. Hu, J. Xu, Y. Gao, Z. Li, J. Shen, W. Wei, Y. Hu, Y. Wu, Y. Wang and M. Ding, *Angew. Chem. Int. Ed.*, 2025, **64**, e202414416.
17. M. Liu, R. Zou and C.-j. Liu, *Appl. Catal. B Environ.*, 2025, **360**, 124549.
18. Y. Li, L. Guo, M. Du, C. Tian, G. Zhao, Z. Liu, Z. Liang, K. Hou, J. Chen, X. Liu, L. Jiang, B. Nan and L. Li, *Nat. Commun.*, 2024, **15**, 5598.
19. T. Li, H. Zhao, L. Guo, G. Liu, J. Wu, T. Xing, T. Li, Q. Liu, J. Sui, Y. Han, J. Liang, Y. He and N. Tsubaki, *ACS Catal.*, 2025, **15**, 1112-1122.
20. M. Tian, X. Tian, E. Ma, J. Hao, Z. Zuo and W. Huang, *ACS Sustainable Chem. Eng.*, 2023, **11**, 13616-13627.
21. J. Shen, X. Cheng, W. Wei, X. Tian and M. Ding, *ACS Catal.*, 2025, **15**, 2402-2414.
22. N. Liu, Q. Fan, J. Wei, G. Zhang, J. Sun, W. Li, C. Song and X. Guo, *ACS Catal.*, 2024, **15**, 179-192.
23. Q. Zhang, S. Wang, R. Geng, P. Wang, M. Dong, J. Wang and W. Fan, *Appl. Catal. B Environ.*, 2023, **337**, 123013.
24. S. Song, H. Song, L. Li, S. Wang, W. Chu, K. Peng, X. Meng, Q. Wang, B. Deng, Q. Liu, Z. Wang, Y. Weng, H. Hu, H. Lin, T. Kako and J. Ye, *Nature Catal.*, 2021, **4**, 1032-1042.
25. V. L. Sushkevich, D. Palagin, M. Ranocchiari and J. A. van Bokhoven, *Science*, 2017, **356**, 523-527.
26. R. Ye, L. Ma, X. Hong, T. R. Reina, W. Luo, L. Kang, G. Feng, R. Zhang, M. Fan, R. Zhang and J. Liu, *Angew. Chem. Int. Ed.*, 2024, **63**, e202317669.
27. J. Moon, Y. Cheng, L. L. Daemen, M. Li, F. Polo-Garzon, A. J. Ramirez-Cuesta and Z. Wu, *ACS Catal.*, 2020, **10**, 5278-5287.
28. S. Eckle, H.-G. Anfang and R. J. Behm, *Appl. Catal. A-Gen.*, 2011, **391**, 325-333.
29. Y. Li, N. Liu, C. Dai, R. Xu, G. Yu, N. Wang, J. Zhang and B. Chen, *Catal.*, 2021,

11, 1444.

30. C. Qi, Y. Bi, H. Yu, H. Zhang, Q. Zhang, X. Wang, M. Fan, T. Xing, M. Wang, M. Wu and W. Wu, *Ind. Eng. Chem. Res.*, 2024, **63**, 9576-9583.
31. X. Liu, P. Si, Y. Zhang, L. Cui, Y. Feng, T. Wang, M. Zhao, F. Liu and F. Han, *Ind. Eng. Chem. Res.*, 2024, **63**, 1170-1178.
32. J. Wu, S. Song, L. Wang, R. Li, J. Wen, Y. Guo, J. Ding, D. Mei, H. Wan and G. Guan, *Chem. Eng. J.*, 2024, **499**, 156439.
33. P. Ye, G. Miao, D. Ray, Z. Tang and C. Song, *ACS Sustainable Chem. Eng.*, 2025, **13**, 7532-7540.
34. L. Wang, Y. Wang, L. Fan, H. Xu, B. Liu, J. Zhang, Y. Zhu and X. Tu, *Chem. Eng. J.*, 2023, **466**, 143347.